Comprehensive quantification of Ni–Gd$_{0.1}$Ce$_{0.9}$O$_{1.95}$ anode functional layer microstructures by three-dimensional reconstruction using a FIB/SEM dual beam system

Kang Taek Lee [a,b], Nicolas J. Vito [b], Eric D. Wachsman [a,*]

[a] University of Maryland Energy Research Center, University of Maryland, College Park, MD 20742, USA
[b] Department of Materials Science and Engineering, University of Florida, Gainesville, FL 32611, USA

HIGHLIGHTS

► We reconstruct Ni–GDC anode functional layers in 3D using a FIB/SEM dual beam system.
► 3D reconstruction allows to quantify various microstructural properties of AFLs.
► The optimal composition of the Ni–GDC AFL is observed at ∼49 vol% Ni AFL.
► TPB density shows an inverse proportionality to the measured electrode ASR.

ARTICLE INFO

ABSTRACT

The Microstructure of Ni–GDC anode functional layers (AFLs) for lower temperature solid oxide fuel cells (SOFCs) were investigated. AFLs with various Ni–GDC compositions (50–80 wt% NiO in AFL before reduction) were quantified by a 3D reconstruction technique using a focused ion beam (FIB)/scanning electron microscope (SEM) dual beam system. Each AFL sample was sectioned into 150 slices with 60 nm intervals. Amira software allowed for alignment, segmentation, and reconstruction of the 2D SEM images into a 3D image. From these reconstructions, volume fractions, effective particle size, phase gradient, and surface area for Ni, GDC, and pore phases were quantified. The estimated phase volume fraction was well matched with the theoretical value. The optimal effective particle size and highest surface area was observed at 49 vol% Ni AFL. The active triple phase boundaries were calculated based on the connectivity of voxels for each phase. The highest TPB density was also achieved at 49 vol% Ni AFL which is a 1:1 volume ratio of Ni to GDC phase. The TPB density shows an inverse proportionality to the electrode ASR measured from SOFC operation.

1. Introduction

The anode supported SOFC design has been widely studied due to its ability to accommodate an ultra thin electrolyte on a thick anode [1–3]. In order to achieve high performance, electrode polarization losses at the anode should be reduced and microstructure greatly influences the electrode polarization. Moreover, the volume fraction of each component in the electrode modifies its microstructure [4]. It is expected that at the optimal SOFC anode composition the number of reaction sites, density of triple phase — electronic conductor, ionic conductor, and gas diffusion path — boundaries (TPBs), is highest. Several studies have been conducted to estimate TPB length and density by stereological methods using analysis of 2D SEM images [4,5]. However, accuracy of active TPB length is limited due to phase interconnectivity issues, which are a three-dimensional (3D) property. Recently, 3D reconstruction techniques were employed to obtain microstructural analysis of SOFCs using a focused ion beam (FIB)/SEM dual beam system [6–12] as well as X-ray nano computed tomography (nano-CT) [13,14]. Using these techniques, more accurate and realistic quantifications of the SOFC electrode microstructure are available. However, these studies were conducted for SOFC cathodes [7–9,11,13] or Ni–YSZ anodes [6,10,14,15] for intermediate to high temperature (>700 °C) SOFC applications. For example, Smith et al. reported that for the LSM–YSZ cathode the charge transfer and

* Corresponding author. Postal Address: 1206 Engineering Lab Bldg, University of Maryland, College Park, MD 20742, USA. Tel.: +1 301 405 8193; fax: +1 301 314 8514.
E-mail address: ewach@umd.edu (E.D. Wachsman).

adsorption polarization (evaluated by deconvolution of impedance) have a logarithmic dependence on TPB density and surface area, respectively [8].

Previously we reported that tailoring the composition of the anode functional layer (AFL) changes the electrochemical performance and power density of the SOFC [16]. In that study a 60 wt% of NiO in NiO–$Ce_{0.9}Gd_{0.1}O_{1.95}$ (GDC) AFL, which is a 1:1 volume ratio of Ni ($\sim$49 vol%) to GDC phase after reduction, exhibited the highest maximum power density (MPD) at intermediate to low temperatures ($\sim$1.15 W cm^{-2} at 650 °C). Moreover, the AFL composition and electrode area specific resistance (ASR) showed an inverse linear relation to MPD. In this study, the microstructural features of Ni–GDC AFLs from the previous study [16] are investigated by 3D reconstruction using a FIB/SEM dual beam system. After reconstruction, comprehensive quantification of microstructural properties is conducted and the values analyzed. Finally, the active TPB density is calculated and related to electrochemical performance.

2. Experimental procedures

2.1. Fuel cell fabrication

NiO–GDC anode-supports were fabricated by tape-casting. The composition of the anode support was fixed at 65 to 35 wt% NiO (Alfa Aesar) to GDC (Rhodia). In an ethanol solvent, an appropriate binder system was prepared with Solsperse, di-n-butyl phthalate (DBP) and poly-vinyl buteral (PVB) as the dispersant, plasticizer, and binder respectively. For homogeneity of the slurry and tape casting strength, the binder system was mixed with the powder mixture and ball-milled for 24 h. After a de-air step, a Procast tape casting system (DHI, Inc) produced a NiO–GDC anode tape. To make button type fuel cells, the dried tape was punched out into 32 mm diameter circles and pre-sintered at 900 °C for 2 h.

AFLs were deposited by a simple colloidal deposition process. To establish a finer structure than the anode support, submicron-sized NiO from J.T.Baker was used with nano-sized GDC from Rhodia. The powder mixture was ball-milled in an ethanol based solvent system for 24 h. The AFL layer was spin coated on the pre-sintered anode surface. In this work four AFL samples were prepared with 50, 60, 65, and 80 wt% NiO. A sample without an AFL was also fabricated as a reference.

Thin and uniform GDC electrolytes were spin-coated on the anode substrates after the AFL deposition. The same Rhodia GDC powder used in the AFL was ball-milled for 24 h with dispersant in an ethanol based solution. PVB and DBP were added to the solution as a binder and a plasticizer and the slurry was ball-milled for an additional 24 h. After milling, the GDC electrolyte layer was deposited by spin coating at 1500 rpm for 20 s. After drying at room temperature for 20 min, the multilayer anode/AFL/electrolyte was co-sintered at 1450 °C for 4 h.

$La_{0.6}Sr_{0.4}Co_{0.2}Fe_{0.8}O_{3-\delta}$ (LSCF) from Praxair–GDC from Rhodia mixture with a 1:1 wt% ratio was used for the cathode. The LSCF–GDC power was mixed with alpha-terpineol, DBP, PVB and ethanol, brush-painted onto the GDC electrolyte, and heat treated at 1100 °C for 1 h. The cathode area was $\sim$0.4 cm^2 after firing.

2.2. Electrochemical characterization

Before 3-D reconstruction of the samples I–V measurement was performed on a Solartron 1407E at temperatures from 450 to 650 °C and Impedance spectroscopy measurements with a Solartron 1400 and a two-point probe were carried out. All measurements were conducted at the frequency range 100 kHz to 100 mHz with ac signal strength of 50 mV under open-circuit voltage (OCV)

conditions. The gas environment for all measurements was fixed with 90 sccm of hydrogen (3% wet) and dry air at the anode and cathode, respectively. The detailed results of the electrochemical performance have been discussed elsewhere [16].

2.3. 3D-Reconstruction

After electrochemical testing, all samples were mounted in an epoxy support using a Struers EpoVac System. This epoxy infiltrates into the samples and fills open pores inside the Ni–GDC anode/AFL structures, providing better contrast for SEM imaging. The sample stub was subsequently ground and polished using sandpaper and diamond paste down to 1 μm roughness to obtain an even surface exposing the anode–electrolyte interface.

The automated sectioning and imaging were carried out with a FIB/SEM dual beam system (FEI Strata DB 235). As shown in Fig. 1a, the electron beam pole (SEM) is inclined 52° to the ion beam pole (FIB). Fig. 1b is a schematic diagram of the 3D reconstruction process. The image of each slice was captured by the SEM. To get better contrast difference between the phases, a through-lens-detector (TLD) in backscatter mode was utilized. Using the FIB a trench was generated around the region of interest (ROI). The slicing distance (z-axis resolution) was 60 nm. To avoid charging during SEM imaging and protect the sample from ion damage, protective platinum layers were deposited with an in-situ liquid metal-organic ion source (LMIS). The repeated imaging and slicing processes were automatically controlled using Auto Slice and View software (FEI Company).

After collecting the cross-sectional images for each sample, the alignment, segment, cropping and labeling for the 3D reconstruction were conducted by Amira software–ResolveRT™ (ver 4.0, Mercury Computer System Inc.) (Fig. 1b). Amira was also utilized to quantify the various microstructural features from the 3D reconstructions of the samples, such as each phase (Ni, GDC, and pore) volume and surface area, phase gradient, tortuosity of pores, and TPB density.
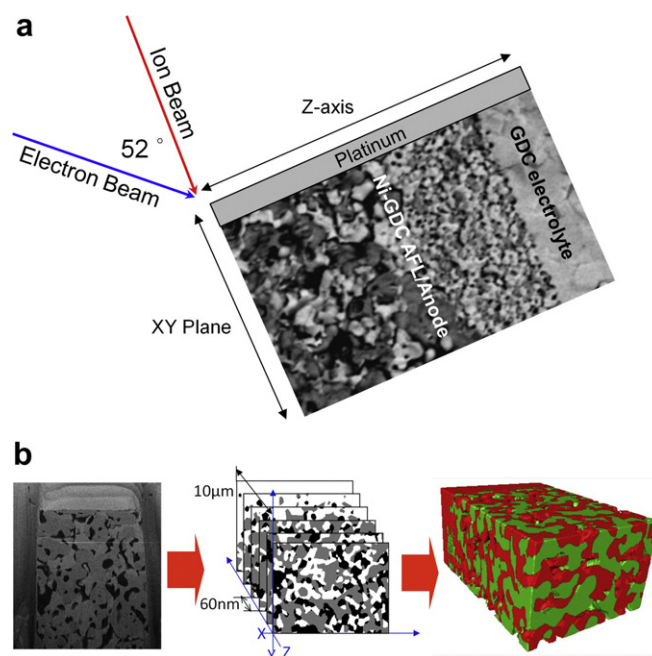
Fig. 1. Schematic diagrams of (a) ion and electron beam setup with a SOFC sample and (b) 3D reconstruction process consisting of 3 steps; (1) serial sectioning and 2D image capturing, (2) alignment, cropping and segmentation, (3) 3D reconstruction.

3. Results and discussion

Fig. 2 shows 3D reconstructions of the cells for direct qualitative comparisons between the anode/AFL structures. The z-axis dimension reconstructed for each sample is approximately 8–10 μm from the GDC electrolyte interface. Considering the AFL thickness (∼10 μm), the analyzed AFL depth in this study is essentially the full cross-section of each AFL [16]. The detailed dimensions for the reconstructed samples are summarized in Table 1.

Compared to the sample with no AFL (Fig. 2a), cells with AFLs (Fig. 2b–e) show much smaller particulate structures. Among the AFLs, the change in amount of Ni (green in 3-D reconstruction) and

GDC (red in 3D reconstructions) is consistent with initial NiO wt%. This result is in good agreement with 2D SEM image observation discussed in previous work [16]. Moreover, this 3D reconstruction allows the separation of each phase or the combination of any two phases. As illustrated in Fig. 3, each of GDC, Ni, pore phase, and combination of Ni-pore phases were individually reconstructed. From this phase separation, the quantification of phase gradient, volume fraction, and surface area for each phase were determined.

The phase volume fractions for Ni, GDC and pore were quantified using the Amira™ tissue-statistics module. The number of voxels for each phase were counted and based on this result the numerical volume fraction for each phase was calculated. The theoretical volume fractions of Ni, GDC and pore after SOFC
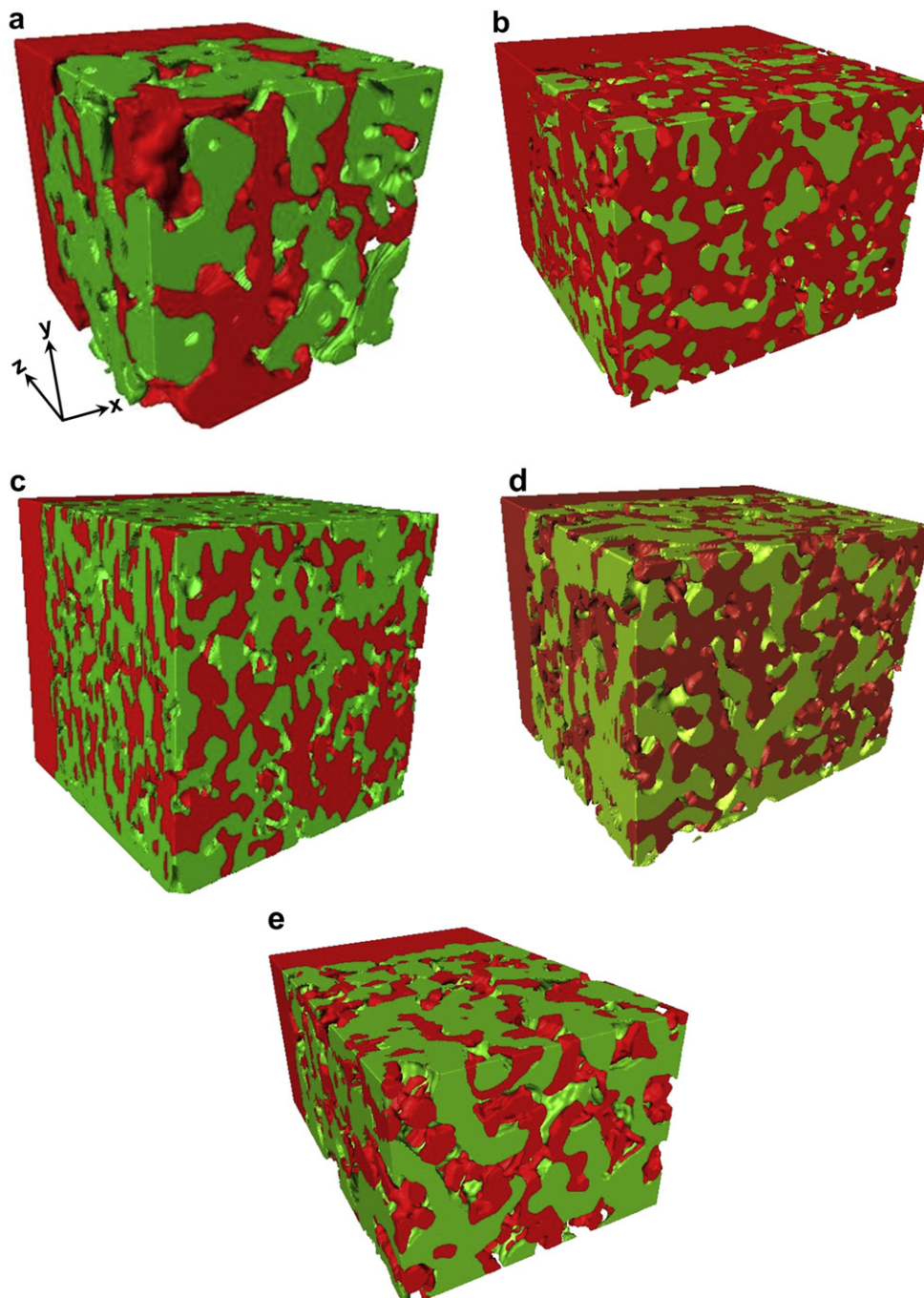

Fig. 2. 3D reconstructions of Ni(green)–GDC(red) (a) anode without AFL, and AFLs with initial composition of (b) 50, (c) 60, (d) 65, and (e) 80 wt% NiO near to AFL(or anode)/electrolyte interface after electrochemical testing. (For interpretation of the references to colour in this figure legend, the reader is referred to the web version of this article.)

Table 1
3D reconstruction dimensions and total volume fractions of Ni, GDC and pore phase and solid volume fractions of Ni and GDC for the AFLs with different NiO wt% in SOFC samples after electrochemical testing at 600 °C.

| Initial AFL composition	NiO (wt%)		50	60	65	80
	GDC (wt%)		50	40	35	20
3D Reconstruction dimension	X (μm)		12.95	8.75	10.45	10.42
	Y (μm)		10.22	6.06	7.95	7.88
	Z (μm)		8.90	10.64	10.76	9.32
	Total reconstructed volume (μm³)		1177.91	564.21	893.91	765.26
Phase volume after reduction	Ni in total volume (%)	Theoretical	30.4	36.3	39.2	47.7
		Measured (SD)	29.1 (±1.0)	37.8 (±5.9)	43.2 (±6.7)	51.1 (±6.4)
	GDC in total volume (%)	Theoretical	48.3	38.4	33.4	19.0
		Measured (SD)	54.6 (±3.0)	40.6 (±4.8)	35.0 (±5.5)	20.0 (±5.9)
	Pore in total volume (%)	Theoretical	21.2	25.3	27.4	33.3
		Measured (SD)	16.3 (±2.9)	21.6 (±3.0)	21.8 (±3.2)	28.9 (±2.9)
	Ni in solid volume (%)	Theoretical	38.6	48.6	53.9	71.6
		Measured (SD)	34.8 (±1.0)	48.1 (±6.7)	55.1 (±7.3)	71.9 (±8.0)
	GDC in solid volume (%)	Theoretical	61.4	51.4	46.1	28.4
		Measured (SD)	65.2 (±1.0)	51.9 (±6.7)	44.9 (±7.3)	28.1 (±8.0)

*SD; standard deviation.

operation condition were estimated assuming full reduction of NiO into Ni. The theoretical and measured values of total volume fraction of each phase for the different AFLs are tabulated in Table 1 and plotted in Fig. 4a. The Ni contents and porosity in the AFL increase with increasing initial NiO wt%, while GDC is inversely proportional to the initial NiO wt% in the AFL. The results clearly show that the Ni and GDC volume fractions extracted from the 3D reconstruction are

well matched with the theoretical values. For example, the measured volume fractions of Ni are 29.1 ± 1.0, 37.8 ± 5.9, 43.2 ± 6.7 and 51.1 ± 6.4 vol% for 50, 60, 65, and 80 wt% NiO AFL samples, respectively, which is very close to the theoretical values of 30.4, 36.3, 39.2, and 47.7 vol% (Table 1.). However, the porosity is slightly below the theoretical value, which might be attributable to sample shrinkage as the NiO is reduced to Ni.
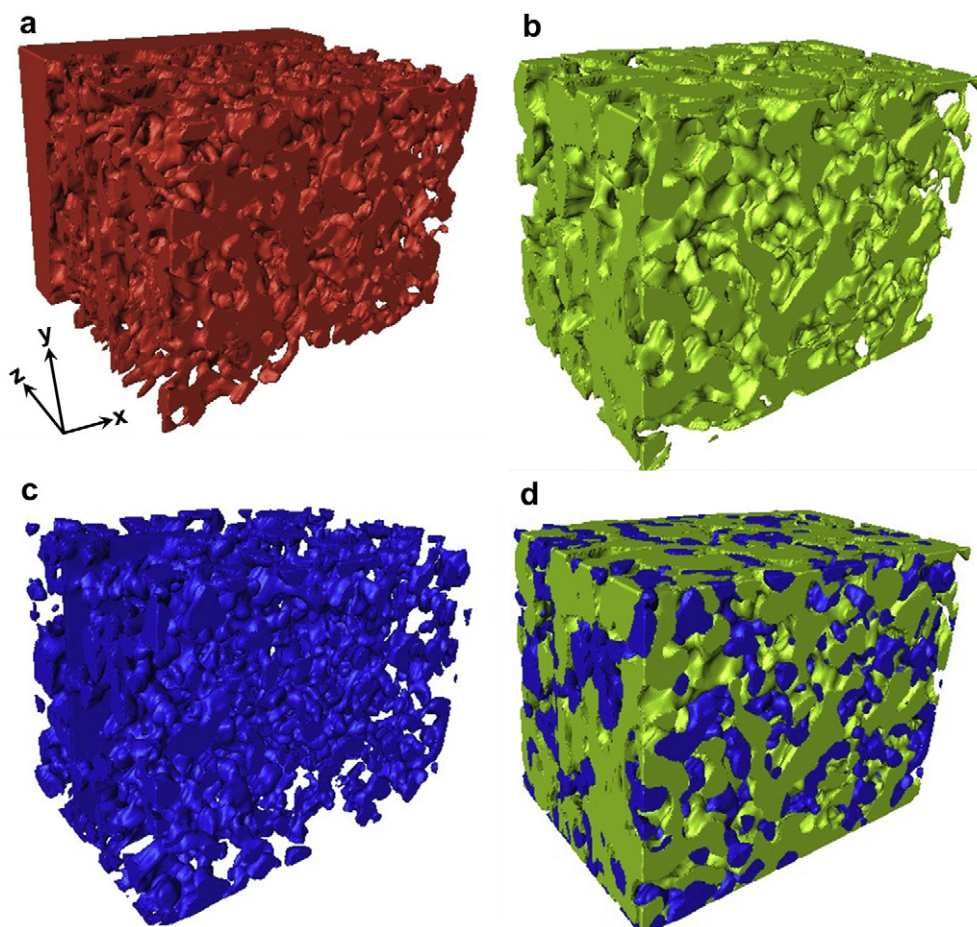
Fig. 3. Individually reconstructed phases from the 3D reconstruction of AFL with 65 wt% NiO; (a) GDC (red), (b) Ni (green), (c) pore (blue), and (d) combination of Ni and pore phases after electrochemical test. (For interpretation of the references to colour in this figure legend, the reader is referred to the web version of this article.)
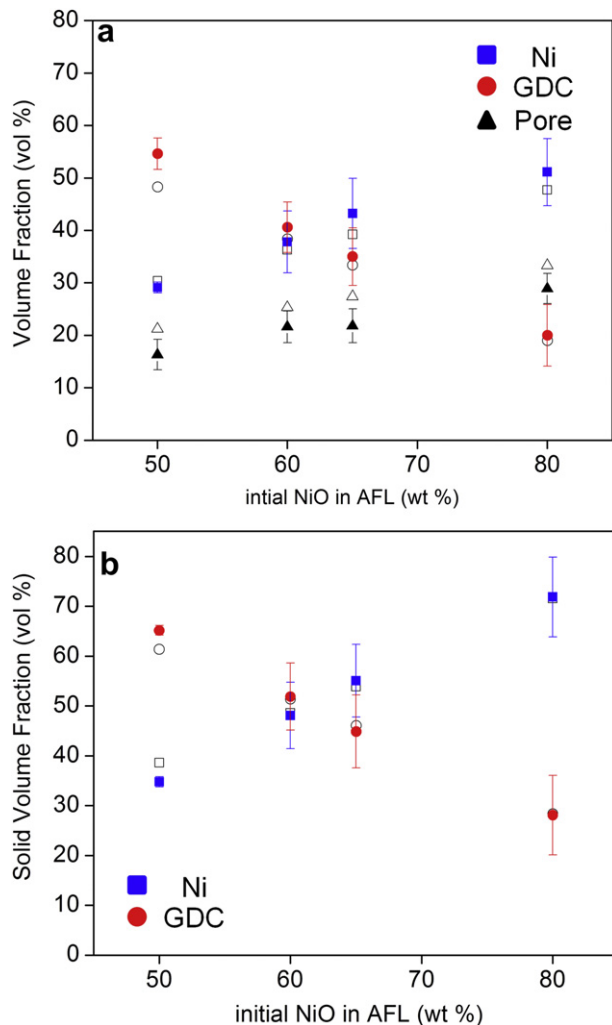
Fig. 4. Volume fraction of Ni (square), GDC (circle) and pore (triangle) phase in total volume (a), and volume fraction of Ni and GDC in solid volume of AFLs with various compositions after electrochemical characterization. Open symbols represent theoretical values.

The solid phase volume fractions (GDC_{sol}, Ni_{sol}) between GDC and Ni were also calculated (Fig. 4b). The estimated solid Ni volumes were 34.8 ± 1.0, 48.1 ± 6.7, 55.1 ± 7.3 and 71.9 ± 8.0 vol% for 50, 60, 65, and 80 wt% NiO AFL samples, respectively. As expected from the theoretical value, at 60 wt% NiO AFL the Ni_{sol} to GDC_{sol} volume ratio was almost 1:1 which is the ratio that had the highest electrochemical performance among studied samples in previous work [16].

Fig. 5 shows the phase distribution as a function of distance for each AFL sample. As expected in Fig. 5b–e the level of Ni and pore phase increases as the amount of NiO increases and GDC phase decreases. In addition, all of the AFL samples have a very narrow transition region (∼below 500 nm) for onset of the GDC phase increase near the GDC electrolyte, compared to over 2000 nm for the bare anode (Fig. 5a). This result indicates a very fine microstructure in the AFL, and that its features such as high surface area and large amount of reaction sites (TPBs) are well retained at the AFL/electrolyte interface. In contrast, the anode without an AFL loses reaction sites (TPBs) and gas diffusion paths due to penetration of the GDC electrolyte into large anode pores at the interfacial zone which is known to be the most important active region for fuel oxidation.

The total surface area values of the AFL structures with different Ni contents were calculated using the Amira tissue statistics

module. The resultant values are normalized by the total volume of the region of interest (ROI) (Table 2).

The effective particle or pore diameters (d) after reduction for each AFL composition were calculated with the Brunauer–Emmett–Teller (BET) method using a general formula written as;

$$d = 6\frac{V}{S} \tag{1}$$

where V and S are the volume and surface area of each phase, respectively. The phase volume and surface area of Ni, GDC and pore in each sample were also calculated. The effective diameters of Ni (d_{Ni}) phase in 50, 60, 65 and 80 wt% NiO AFL correspond to 683, 771, 917, and 1120 nm, respectively, showing the expected trend. The complete data set is tabulated in Table 2 and plotted in Fig. 6. A linear relationship between effective diameter and AFL composition is obtained for all three phases which is proportional for Ni and porosity, and inversely proportionality for GDC. This indicates that a high Ni content in the AFL produces a structure with large Ni particles and very small GDC particles, which can cause poor connectivity of the smaller particle phase (GDC) and decreasing effective TPB sites. In contrast, for a low Ni AFL the opposite situation for the solid phase occurs but is worse due to lower porosity, which interferes with the fuel gas diffusion. Therefore, it is expected that an initial NiO AFL content of 55–60 wt% is optimal for the highest TPB density. However, powder particle size should also be considered with other factors, such as composition and porosity. In addition, it is interesting that the effective diameter of each phase in multiphase materials varies significantly with relative composition (Table 2) even though initial starting material diameters were identical. This implies that, if one develops an electrochemical micro-model of an electrode, the feature sizes (or effective diameters) cannot be simply assumed based on the initial particle sizes but should be evaluated in an appropriate way.

The tortuosity (τ) was estimated using the moment of inertia module in the Amira software. Using this module, tracking of the center of the open pore phase through sample from the beginning of the AFL to the GDC electrolyte interface was performed, which allowed us to measure the accumulated 3D Euclidian distance through the region. The accumulated Euclidean distance divided by AFL thickness yielded the tortuosity of each sample (Table 2). For the 50, 60, 65, and 80 wt% NiO AFL, the tortuosity values were 2.77, 1.91, 1.91, and 1.69, respectively (Fig. 7). These results are comparable with reported tortuosity values (1–3) for modern SOFC materials, and is within the most physically reasonable range [17]. This result is in good agreement with the pore volume fraction data (Fig. 4a) and the general theory that higher porosity with larger pore diameter provides less tortuous gas diffusion paths through the open pores. In addition, this tortuosity can be combined with the volume fraction of porosity to estimate the effective diffusion coefficient (D_{eff}), which is directly related to concentration polarization [8,18] written as;

$$D_{eff} = D\frac{V_{pore}}{\tau'} \tag{2}$$

where the D, V_{pore}, and τ' are diffusion coefficient, volume fraction porosity, and tortuosity factor, respectively. Recently Schmidt and Tsai reported that through the calculation of effect of anode tortuosity on fuel and exhaust gas flow, the tortuosity factor (τ') corresponds to square of tortuosity (τ^2) [17]. As shown in Fig. 7, the $V_{pore}/(\tau^2)$ increases with Ni content in the AFL. This should therefore cause higher concentration polarization at low Ni content AFLs.

The percolative TPB density for each AFL composition was also quantified. While the TPB site is where the three phases Ni, GDC,
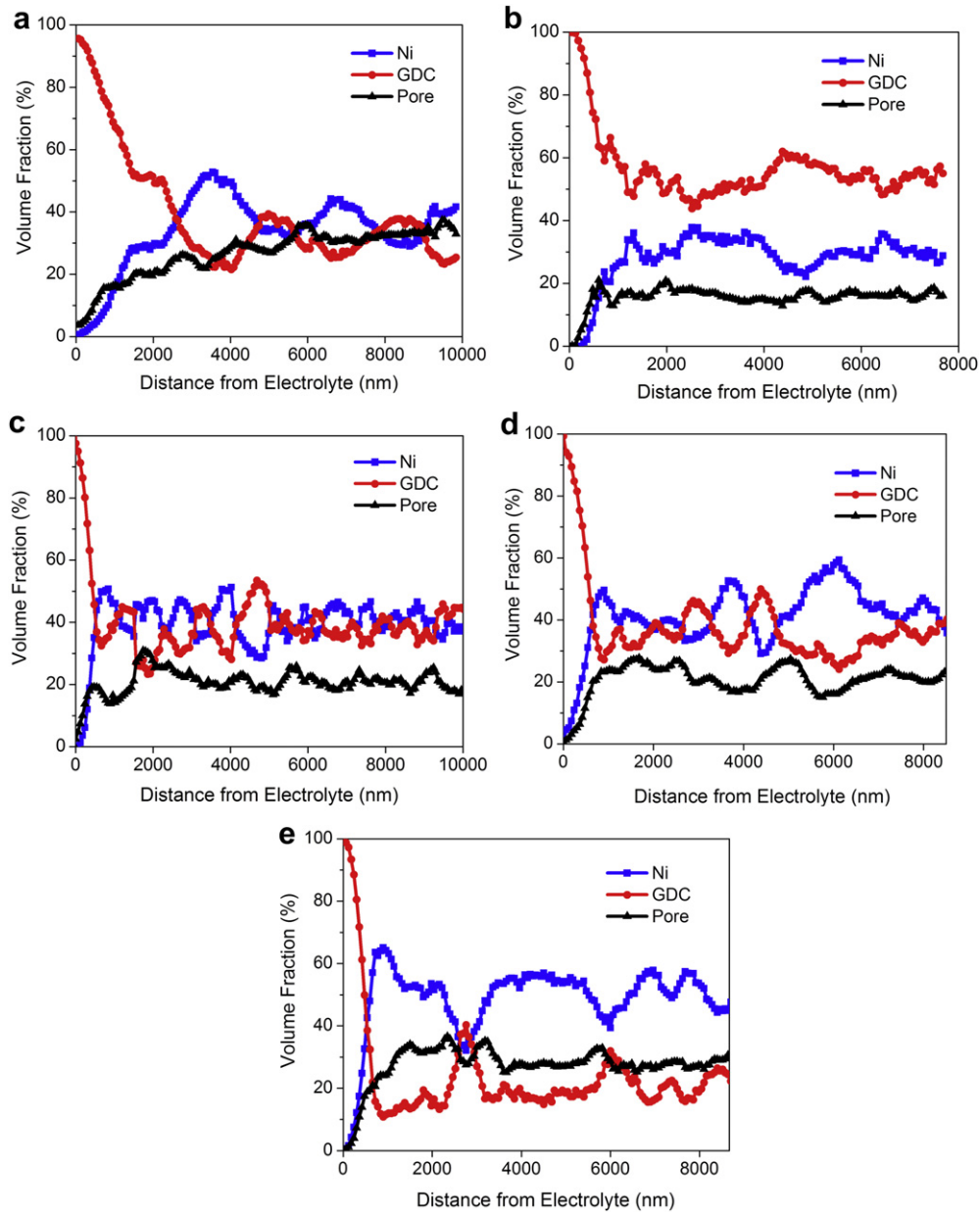
Fig. 5. Phase gradient plots of the reconstructed samples with (a) no AFL, (b) 50, (c) 60, (d) 65, and (e) 80 wt% NiO in AFL after electrochemical test. Square, circle, and triangle symbols represent Ni, GDC, and pore phases, respectively.

and pore meet, it is active only when these phases percolate continuously through the structure. For example, the GDC phase of a TPB site should be connected to the GDC electrolyte to make a path for oxygen ions from the anode(AFL)/GDC electrolyte interface to the active site. At the same time, the Ni phase and pores should have percolation to the interconnect (or current collector) and fuel channel (outside anode), respectively, in order to bring the fuel to the TPB sites, to conduct charge transfer during fuel oxidation at the TPB, and to complete the extraction of electrons from the reaction site to the outside circuit. Therefore, counting the active TPB and removing the inactive (or dead) TPB from the total TPB measurement is a critical issue [10,12].

The TPB density was calculated based on identification of the voxels and their connectivity (Fig. 8). During the 3D reconstruction process, every voxel was label as one of the phases: GDC, Ni, and pore. Generally one edge is shared by 4 voxels and if an edge is shared by all 3 phases, it is counted as part of the TPB length. In

order to estimate the actual working TPB density, the TPB sites were classified into 3 categories, which are active, inactive, and unknown. The connectivity of each phase at the TPB was traced along xy, yz, and zx planes. If the Ni, GDC and pores are connected across the AFL from the GDC electrolyte interface to the outside end of the AFL it was counted as 'active'. If one of the phases connected to the TPB site was isolated inside the reconstructed region, it referred to as 'inactive'. Other cases (e.g., extending outside of the reconstruction region) are sorted as 'unknown'. The total TPB length (L_{TPB}) was estimated by summation of the length of the voxel edges counted as active TPB. The TPB density (ρ_{TPB}) is calculated by

$$\rho_{TPB} = \frac{L_{TPB}}{V_{total}} \tag{3}$$

where the V_{total} is the total volume of ROI. The unit of TPB density is μm^{-2} ($=\mu m/\mu m^3$). For unknown TPBs, it was

Table 2
Summary of quantification of microstructural features of AFLs with various compositions.

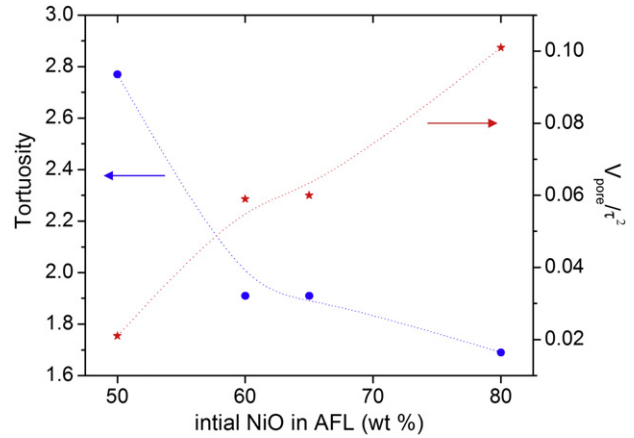| Initial NiO composition in AFL	(wt%)	50	60	65	80
Effective Ni diameter, d_{Ni}	(nm)	683	771	917	1120
Effective GDC diameter, d_{GDC}	(nm)	890	642	650	316
Effective Pore diameter, d_{pore}	(nm)	381	452	489	560
Surface area per volume, SA/V	(μm^{-1})	2.4	2.9	2.4	2.6
Tortuosity, τ	(N/A)	2.77	1.91	1.91	1.69
TPB density, ρ_{TPB} (SD)	(μm^{-2})	8.5 ($\pm$1.4)	15.6 ($\pm$5.0)	14.2 ($\pm$3.4)	6.3 ($\pm$2.3)
Electrode ASR at 600 °C	(Ω cm^2)	0.48	0.38	0.41	0.66

assumed that the same connectivity of the each phase exists out of the ROI and the unknown TPBs have the same portion of active and dead TPBs as in the known region. Based on this assumption, the total active TPB density ($\rho_{TPB,\,active,\,total}$) was estimated by

Fig. 6. Effective particle diameters of Ni (square), GDC (circle), and pore (triangle) phase of AFLs with various compositions after electrochemical test. The dotted line is the linear fit for each phase.

Fig. 7. Tortuosity (circle) and V_{pore}/τ^2 (star) of samples after electrochemical test plotted as a function of initial NiO contents. The lines are only to guide the eye.

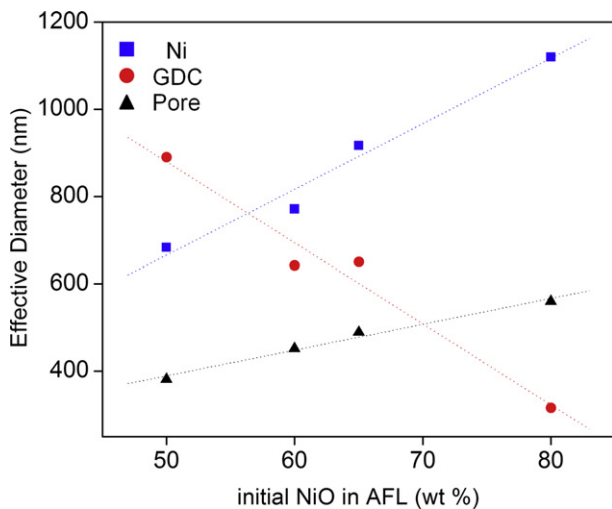$$\rho_{TPB,active,total} = \frac{L_{TPB,active}}{V_{total}}\left(1 + \frac{L_{TPB,unknown}}{L_{TPB,active} + L_{TPB,dead}}\right) \quad (4)$$

where the $L_{TPB,\,active}$, $L_{TPB,\,dead}$, and $L_{TPB,\,unknown}$ are active, dead, and unknown TPB length in a measured volume, respectively. The calculated total active TPB densities were 8.5 $\pm$ 1.4, 15.6 $\pm$ 5.0, 14.2 $\pm$ 3.4, and 6.3 $\pm$ 2.3 μm^{-2}, respectively (Table 2).

Fig. 9 shows the TPB density and surface area per volume as a function of NiO content in the AFLs. As expected from total surface area and effective particle size analysis discussed above, the highest TPB density was achieved in an AFL with 60 wt% NiO (49 vol% Ni$_{sol}$, a ~1:1 volume ratio of Ni to GDC). However, the TPB standard deviation is greater for higher TPB values. This might reflect that the AFL with larger TPB density has higher randomness and a more complicated structure. The high scattering of the TPB density can be reduced by introducing computational simulation methods [12] or a morphological correction factor [11].
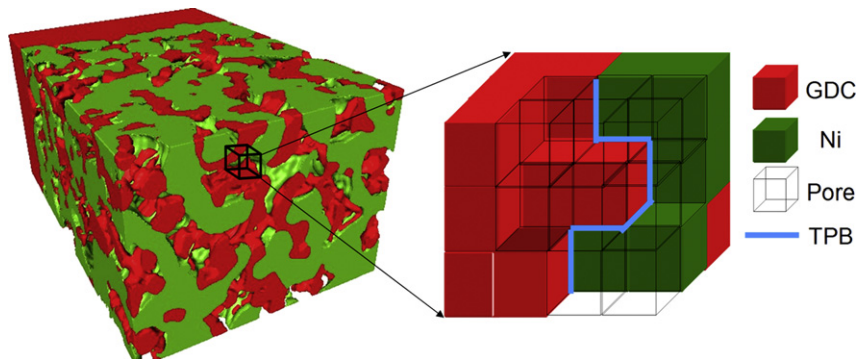
For surface area, a similar trend to TPB density is found over the range from 50 to 65 wt% NiO. The maximum surface area is similarly reached at 60% NiO AFL, in good agreement with results from other studies that the higher surface area produces higher TPB density [5,7]. However, at higher NiO the surface area value levels off and actually appears to increase. This is due to the highly porous structure after reduction of NiO to Ni, and the greater increase in effective Ni diameter with NiO content. In addition, it should be noted that in this study the effective particle size and porosity was


Fig. 8. Schematic diagram of TPB length calculation from 3D reconstruction. A rectangular parallelepiped represents a voxel in a 3D reconstruction and each one is labeled as one of the phases; Ni (green), GDC (red), or pore (open) phase. An edge which is shared by all three other phases is counted as a TPB length (blue line). (For interpretation of the references to colour in this figure legend, the reader is referred to the web version of this article.)
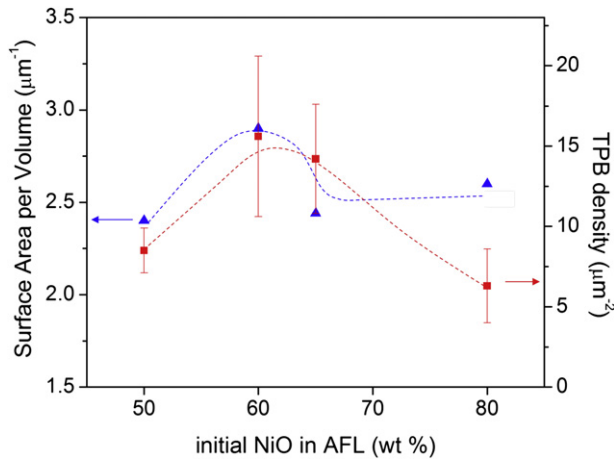
Fig. 9. Plot of quantified surface area (triangle) and TPB density (square) of AFLs with various initial NiO contents. The lines are only to guide the eyes.

controlled only by AFL compositional change and accompanying volume fraction change upon NiO reduction, while in other studies the phase composition of the electrodes were fixed while particle size was actively changed.

Finally the effect of TPB density on electrochemical performance was determined by, electrochemical impedance spectroscopy under OCV conditions. Fig. 10 shows the Nyquist plots of SOFCs with the various AFL compositions. For comparison purposes, the ohmic
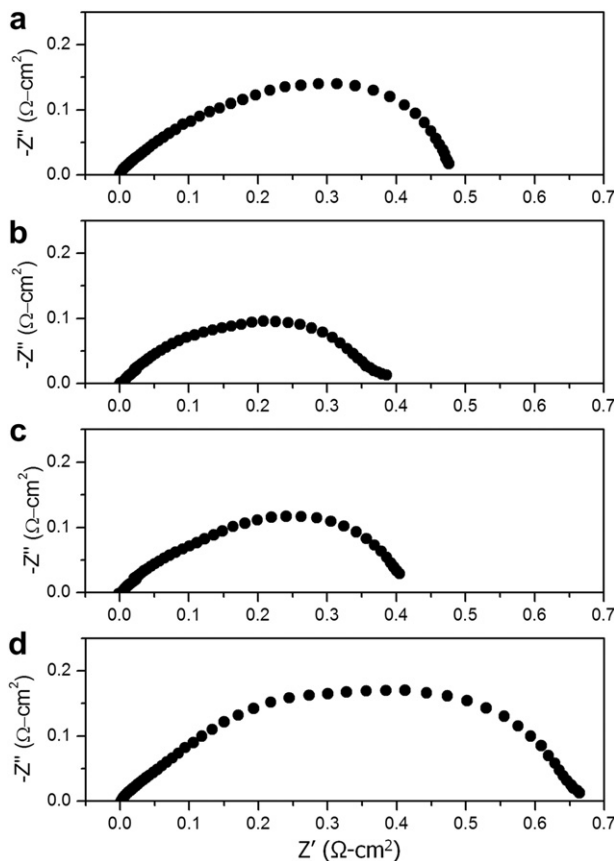
Fig. 10. Impedance spectra of SOFC samples with (a) 50, (b) 60, (c) 65, and (d) 80 wt% NiO in AFL. The impedance test was conducted at 600 °C over the range of 100 kHz to 100 mHz under open circuit condition.
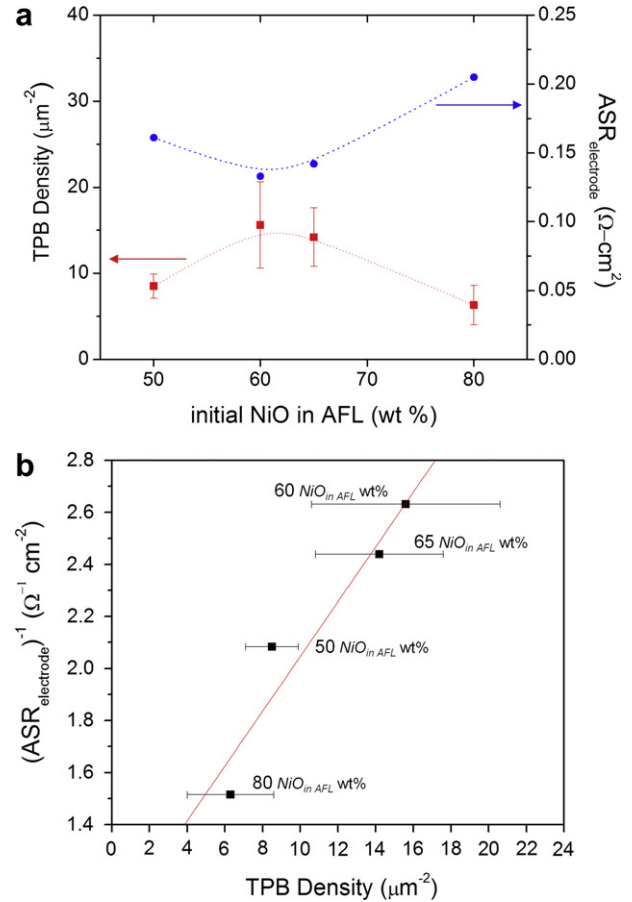
Fig. 11. (a) TPB density (square) and electrode ASR (circle) with various AFL compositions (Dotted lines are only for guiding purposes.) (b) Plot of reciprocal electrode ASR with TPB density. A red line represents the linear fit for the plot showing the inverse relationship between TPB and electrode ASR. (For interpretation of the references to colour in this figure legend, the reader is referred to the web version of this article.)

resistance was removed. The non-ohmic electrode ASR ($ASR_{electrode}$) was estimated as the value between the high frequency and low frequency intercepts (Table 2). It is assumed that the cathode ASRs were essentially identical since all of the cathodes were processed the same. Therefore, the $ASR_{electrode}$ trend is due to the anodic ASR change.

Fig. 11a shows the TPB and $ASR_{electrode}$ as a function of AFL composition. The TPB density exhibits an inverse trend with $ASR_{electrode}$. Previously, Bieberie et al. reported that the primary electrode process depends on TPB density [19]. Using a patterned Ni anode as a model electrode, they showed that the electrode polarization under open circuit condition is correlated to TPB density, which is a linear relationship between inverse resistance and TPB density. Similarly in Fig. 11b our data shows a clear inverse linear relationship between $ASR_{electrode}$ and TPB density. The minor deviations from the linearity can be caused by scattering of the TPB length from the 3D reconstruction accuracy and the impact of compositional change of the AFL on electrochemical polarization mechanism.

4. Conclusions

In this work, microstructural properties of Ni–GDC anode functional layers for lower temperature SOFCs were quantified by a state-of-the-art 3D reconstruction technique. For 3D reconstruction, each sample was automatically sectioned and each sectional image was acquired using a FIB/SEM dual beam system. After labeling of each image to give phase separation, the series of

sectioned images were incorporated and reconstructed in 3D utilizing the Amira software. From this 3D reconstruction, the phase gradient through the sample depth and volume fraction, effective diameter, surface area for each phases (Ni, GDC, and pore), and pore tortuosity were quantified. This result showed that the volume fraction was well matched with theoretical values. In addition to volume fraction, the graded phase plot showed that the actual AFL/anode structure have some degree of deviation of each phase volume fraction, so the accurate quantification of micro-structural properties could be achieved by bulk analysis. As one of the most important features in the anode microstructure, the active TPB density was evaluated by checking the connectivity of voxels for each phase. The highest TPB length was found at the 1:1 volume ratio of the Ni to GDC in AFL. Moreover, the TPB densities showed an inverse linear relation with electrode ASR.

Acknowledgments

References

[1] S. deSouza, S.J. Visco, L.C. DeJonghe, Solid State Ionics 98 (1997) 57–61.
[2] S.D. Kim, S.H. Hyun, J. Moon, J.H. Kim, R.H. Song, Journal of Power Sources 139 (2005) 67–72.
[3] J.S. Ahn, D. Pergolesi, M.A. Camaratta, H. Yoon, B.W. Lee, K.T. Lee, D.W. Jung, E. Traversa, E.D. Wachsman, Electrochemistry Communications 11 (2009) 1504–1507.
[4] J.R. Wilson, S.A. Barnett, Electrochemical and Solid State Letters 11 (2008) B181–B185.
[5] N. Shikazono, Y. Sakamoto, Y. Yamaguchi, N. Kasagi, Journal of Power Sources 193 (2009) 530–540.
[6] J.R. Wilson, W. Kobsiriphat, R. Mendoza, H.Y. Chen, J.M. Hiller, D.J. Miller, K. Thornton, P.W. Voorhees, S.B. Adler, S.A. Barnett, Nature Materials 5 (2006) 541–544.
[7] D. Gostovic, J.R. Smith, D.P. Kundinger, K.S. Jones, E.D. Wachsman, Electro-chemical and Solid State Letters 10 (2007) B214–B217.
[8] J.R. Smith, A. Chen, D. Gostovic, D. Hickey, D. Kundinger, K.L. Duncan, R.T. DeHoff, K.S. Jones, E.D. Wachsman, Solid State Ionics 180 (2009) 90–98.
[9] J.R. Wilson, A.T. Duong, M. Gameiro, H.Y. Chen, K. Thornton, D.R. Mumm, S.A. Barnett, Electrochemistry Communications 11 (2009) 1052–1056.
[10] J.R. Wilson, M. Gameiro, K. Mischaikow, W. Kalies, P.W. Voorhees, S.A. Barnett, Microscopy and Microanalysis 15 (2009) 71–77.
[11] J.R. Wilson, J.S. Cronin, A.T. Duong, S. Rukes, H.Y. Chen, K. Thornton, D.R. Mumm, S. Barnett, Journal of Power Sources 195 (2010) 1829–1840.
[12] N. Shikazono, D. Kanno, K. Matsuzaki, H. Teshima, S. Sumino, N. Kasagi, Journal of the Electrochemical Society 157 (2010) B665–B672.
[13] P.R. Shearing, R.S. Bradley, J. Gelb, S.N. Lee, A. Atkinson, P.J. Withers, N.P. Brandon, Electrochemical and Solid State Letters 14 (2011) B117–B120.
[14] P.R. Shearing, J. Gelb, N.P. Brandon, Journal of the European Ceramic Society 30 (2010) 1809–1814.
[15] J.S. Cronin, J.R. Wilson, S.A. Barnett, Journal of Power Sources 196 (2011) 2640–2643.
[16] K.T. Lee, N.J. Vito, H.S. Yoon, E.D. Wachsman, Journal of the Electrochemical Society 159 (2012) F187–F193.
[17] V.H. Schmidt, C.-L. Tsai, Journal of Power Sources 180 (2008) 253–264.
[18] Y. Jiang, A.V. Virkar, Journal of the Electrochemical Society 150 (2003) A942–A951.
[19] A. Bieberle, L.P. Meier, L.J. Gauckler, Journal of the Electrochemical Society 148 (2001) A646–A656.